Supplementary Information

Multifunctional 1-Naphthoic Acid Additive Enhancing Ultraviolet Stability of Perovskite Solar Cells

Xu Zheng[a,b], Jiangying Lu[c], Jinyao Wang[a,b], Yulin Wu[a,b], Shan Wu[c], Jingteng Ma[a,b], Yehua Yang[d], Xuan Tang[a,b], Wei Jiang[a,b], Yipeng Xu[a,b], Bilal Mehmood[a,b], Shizhong Yue[a,b]*, Kong Liu[a,b]*, Zhijie Wang[a,b]*, and Shengchun Qu[a,b]*

[a] Laboratory of Solid-State Optoelectronics Information Technology, Beijing Key Laboratory of Low Dimensional Semiconductor Materials and Devices, Institute of Semiconductors, Chinese Academy of Sciences, Beijing, P. R. China, 100083.

[b] Center of Materials Science and Optoelectronics Engineering, University of Chinese Academy of Sciences, Beijing, P.R. China, 100049.

[c] School of Chemistry and Chemical Engineering, Guangxi University, Nanning, P. R. China, 53004.

[d] School of Science, China University of Geosciences, Beijing, P.R. China, 100083.

* Corresponding author:

yueshizhong@semi.ac.cn, liukong@semi.ac.cn,

wangzj@semi.ac.cn, qsc@semi.ac.cn.

Materials and methods

Materials

All the materials are used without further purification. The organic halide salts, methylammonium bromide (MABr), methylammonium iodide (MAI), and formamidinium iodide (FAI) were purchased from Greatcell Solar. Chlorobenzene (CB, 99.8%), anhydrous N, N-dimethylformamide (DMF, 99.8%), anhydrous dimethylsulfoxide (DMSO, 99.8%), bathocuproine (BCP), cesium iodide (CsI, 99.99%), rubidium iodide (RbI, 99.99%), lead(ii) bromide ($PbBr_2$, 99.999%), 1-naphthoic acid (1-NA), 2-naphthoic acid (2-NA), and benzoic acid (BA) were purchased from Sigma-Aldrich. Propane-1,3-diamine dihydroiodide ($PDAI_2$) and methylammonium chloride (MACl) were purchased from Xi'an Yuri Solar Co., Ltd. C_{60} was purchased from Nano-C. Lead(ii) iodide (PbI_2, 99.99%) and [2-(3,6-dimethoxy-9H-carbazol-9-yl)ethyl] phosphonic acid (MeO-2PACz) were purchased from Tokyo Chemical Industry. Acetone, isopropanol (IPA), anhydrous ethanol, and toluene (TL) were purchased from Tianjin Fengchuan Chemical Reagent Co.Ltd.

Device fabrication methods

The FTO substrates (1.5 × 1.5 cm^2) were sequentially washed by sonication with detergent, deionized water, acetone, isopropanol, and ethanol for 30 min. Then, the FTO substrates were treated in an ultraviolet–ozone for 30 min to prepare solar cells. First, the MeO-2PACz was dissolved in ethanol at a concentration of 0.5 mg/mL and spin-coated at 3000 rpm for 30 s. The sample was then annealed at 100 ℃ for 10 min. Then, perovskite precursor solution (1.5 M) was prepared by mixing 5% MACl in DMF: DMSO mixed solvents (4:1, v/v) according to the stoichiometric ratio of $Rb_{0.05}MA_{0.05}Cs_{0.05}FA_{0.85}Pb(I_{0.95}Br_{0.05})_3$. For the additive-treated cells, the 1-naphthoic acid (1 mg/mL) was added to the perovskite precursor solution. After filtered by nylon filters (0.24 μm), the perovskite films were acquired by one-step spin-coating on the MeO-2PACz layer using a spin program of 10 s at 1000 rpm followed by 40 s at 3000 rpm., 160 μL of chlorobenzene was quickly poured to extract the mixed

solvents at the 16th second before the end, and then annealed at 100 ℃ for 10 min. Subsequently, the $PDAI_2$ solution dissolved in mixed solvents (IPA: TL=1:1, v/v) at a concentration of 0.04 mg/mL was spin-coated on the cooled perovskite layer at 3000 rpm for 20 s, followed by annealing at 70 ℃ for 5 min. After cooling down to room temperature, samples were transferred to an Angstrom evaporator for C_{60} (30 nm)/BCP (5 nm)/Ag (100 nm) deposition.

Characterization

J-V characteristics of perovskite solar cells were recorded using a Keithley 2450 Source Meter under 1 sun (AM 1.5 G) illumination using a solar simulator (Newport). Accelerated aging experiments were conducted under continuous illumination using a solar simulator (Perfectlight Technology, PLS-LED100C). The EQE curves were measured using an EnliTech EQE measurement system.

X-ray diffraction patterns were acquired by the X-ray diffractometer (Rigaku SmartLab). Grazing incidence XRD was acquired by the X-ray diffractometer (Rigaku Smartlab 9KW), and the measurement was performed at a grazing incidence angle of $\omega = 0.3$ °. All absorption measurements were carried out by an ultraviolet–visible spectrophotometer (TP-720 UV-VIS-NIR). The morphology of the perovskite surface and cross sections, and Energy-dispersive X-ray spectroscopy were obtained by scanning electron microscopy (SEM, Hitachi SU8020) and energy dispersive spectrometer (EDS, HORIBA EMAX mics2). Surface roughness images were performed with an atomic force microscope (AFM, Bruker Nano Inc ICON2-SYS). Ultrahigh vacuum photoelectron spectroscopy (Thermoescalab 250Xi) was used for XPS measurements. Fourier transform infrared spectroscopy spectra were obtained by an FT-IR spectrometer (Nicolet 6700). Continuous illumination PL spectra information was collected by this objective and sent to the spectrometer (Princeton Acton SP2300i), and a laser (Spectra-physics, central wavelength: 400 nm) was used as the pump source, and continuous illumination aging (15 μW). The water contact angle was measured by a contact angle goniometer (KRUSS DSA).

A FLS1000 spectrometer measured PL spectra. The excitation wavelength was set at 500 nm. Time-resolved PL spectra were measured by an F900 spectrometer with a 375nm pulsed laser (EPL-375). The decay curves were fitted to the bi-exponential equation:

$$\varphi(t) = t_0 + A_1\exp(-t/\tau_1) + A_2\exp(-t/\tau_2) \quad (1)$$

$$\tau_{avg} = (A_1\tau_1^2 + A_2\tau_2^2)/(A_1\tau_1 + A_2\tau_2) \quad (2)$$

where $\varphi(t)$ is the time-dependent PL photon flux, τ_1 represents the fast decay lifetime corresponding to trap-assisted nonradiative recombination and τ_2 represents the slow decay lifetime relating to radiative recombination. PL mapping measurements were performed using an ARsiMP-LSM laser scanning confocal microscope. The samples were excited with a 561 nm laser, and the photoluminescence signals were collected through confocal scanning imaging to obtain spatially resolved PL intensity distributions.

Temperature-dependent conductivity (TDC) was extracted from the current response of a lateral perovskite device, with a configuration of Au/perovskite/Au (0.05 mm gap between Au electrodes), under an applied electrical field of 0.4 V mm^{-1}. The conductivity measurement (Keithley 2400) was performed in N_2 atmosphere with the working temperature controlled by a probe station (Lakeshore EMPX-H2) from 150 K to 300K with a 5 K step. The calculation of E_a is based on the Nernst-Einstein equation:

$$\sigma T = \sigma_0\exp(-E_a/k_BT) \quad (3)$$

where σ_0 is a constant, σ is ionic conductivity, k_B is the Boltzmann constant, and T is temperature.

The space-charge-limited current (SCLC) curves are used to determine the electronic mobility, followed by the device structure of ITO/SnO_2/perovskite/C_{60}/BCP/Ag. About Mott Gurney law, the Ohmic region is at low voltage, the trap-filled limited region is at intermediate voltage, and the trap-filled child region is at high voltage, respectively. The trap density (N_t) can be evaluated by

the formula:

$$N_t = 2\varepsilon_r\varepsilon_0 V_{TFL}/ed^2 \quad (4)$$

where ε_r is the relative permittivity constant of perovskite, ε_0 is the vacuum permittivity, d is the thickness of the perovskite films, and V_{TFL} is the trap-filled limit voltage.

Theoretical Calculation Methods:

Electrostatic potential (ESP). All of the calculations were investigated with the Gaussian 16 software package. Structural optimization and electronic properties were performed using the B3LYP functional with the def2-TZVP basis set (empirical dispersion correction GD3(BJ)).

Frontier molecular orbital energy calculation. All calculations were performed using the DMol3 module within the Materials Studio software package, which is based on density functional theory (DFT). The double numerical plus d-function (DND) all-electron basis set was employed for all atoms. The DND basis set includes one numerical function for each occupied atomic orbital, a second set of functions for valence atomic orbitals, and a polarization d-function on all atoms. The exchange-correlation potential was treated within the local-density approximation (LDA) with the Perdew-Wang (PWC) functional. Upon completion of the geometric optimizations, single-point energy calculations were performed on the optimized structures to obtain the electronic properties. The energies and spatial distributions of the frontier molecular orbitals, specifically the highest occupied molecular orbital (HOMO) and the lowest unoccupied molecular orbital (LUMO), were analyzed to determine the HOMO-LUMO energy gap.

Supplementary Notes

Note 1: Quantitative Analysis of Energy Levels and the Red Shift

As observed in UV-Vis spectra, the absorption features of 1-naphthoic acid (1-NA) and 2-naphthoic acid (2-NA) exhibit a pronounced red shift compared to benzoic acid (BA), along with enhanced absorption in the 300-400 nm range. This phenomenon is a direct consequence of the expanded π-conjugated system resulting from the substitution of the single benzene ring with a larger naphthalene ring.

To quantitatively elucidate this at the electronic level, we performed density functional theory (DFT) calculations to determine the energy levels of the frontier molecular orbitals—the Highest Occupied Molecular Orbital (HOMO) and the Lowest Unoccupied Molecular Orbital (LUMO). The calculated energy levels, the resulting HOMO-LUMO energy gaps, and their correlation with the molecular structures are depicted in **Fig. S2**.

1. Narrowing of the Energy Gap is the Direct Cause of the Red Shift:

The DFT calculations provide a solid theoretical basis for the observed red shift. As shown in the energy level diagram, BA possesses the largest HOMO-LUMO energy gap, $\Delta E = 4.12$ eV. Upon expansion of the conjugated system from a benzene to a naphthalene ring, the energy gap decreases significantly: $\Delta E = 2.97$ eV for 1-NA and $\Delta E = 3.17$ eV for 2-NA. According to the photon energy-wavelength relationship, E_{gap} (eV) = 1240/λ (nm), a smaller energy gap directly corresponds to a lower energy requirement for the electronic transition, resulting in a shift of the absorption wavelength (λ) to longer wavelengths (red shift). This quantitatively explains the red shift of the absorption peak from ~290 nm for benzoic acid to ~350 nm for the naphthoic acids.

2. Energy Level Trends Reveal the Conjugation Effect: The specific changes in energy levels provide further insight into the electronic effects of π-conjugation extension:

Rise in HOMO Energy: Compared to BA (-6.66 eV), the HOMO levels of both naphthoic acids are significantly raised (1-NA: -5.87 eV; 2-NA: -6.15 eV). This indicates that the expanded π-system makes the highest occupied orbital less stable (higher in energy), facilitating electron excitation.

Change in LUMO Energy: Concurrently, the LUMO levels of the naphthoic acids (1-NA: -2.90 eV; 2-NA: -2.98 eV) are slightly lowered compared to BA (-2.54 eV), meaning the lowest unoccupied orbital becomes relatively more stable and easier to reduce.

This combined effect of a "raised HOMO and a lowered LUMO" leads to a significant contraction of the HOMO-LUMO gap, which is the electronic origin of the absorption red shift.

3. Subtle Differences Between Isomers:

The calculation results indicate that the energy gap of 1-NA (2.97 eV) is slightly smaller than that of 2-NA (3.17 eV), primarily due to the higher HOMO energy of 1-NA. This difference may be attributed to subtle variations in intramolecular electron distribution and spatial effects caused by the distinct positions of the carboxyl group on the naphthalene ring, leading to minor differences in their photophysical properties.

The combination of theoretical calculations and experimental spectroscopy quantitatively confirms that the absorption red shift from benzoic acid to naphthoic acids originates from the effective narrowing of the HOMO-LUMO energy gap by the extended π-conjugated system of the naphthalene ring. The DFT calculations not only reproduce the trend of gap reduction but also clearly illustrate the specific mechanism: a significant elevation of the HOMO energy coupled with a slight lowering of the LUMO energy.

Supplementary Figures

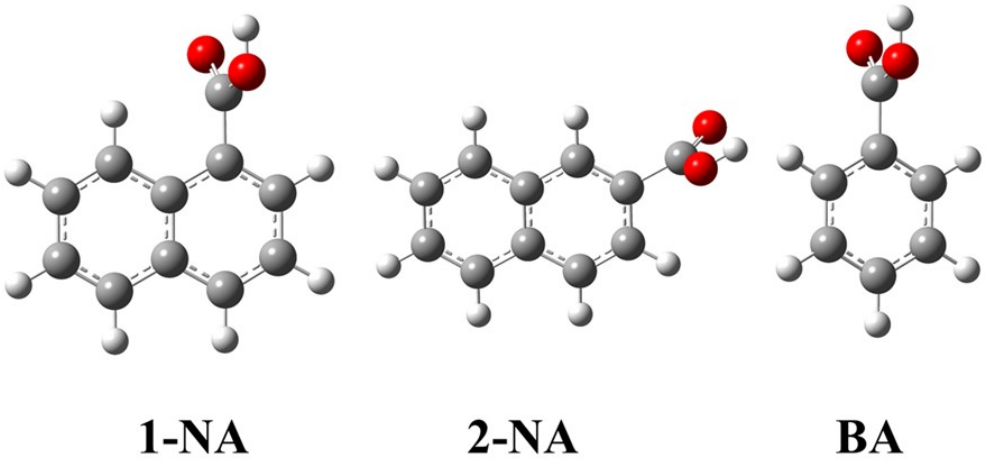

Fig. S1. The structure of 1-NA,2-NA, and BA.

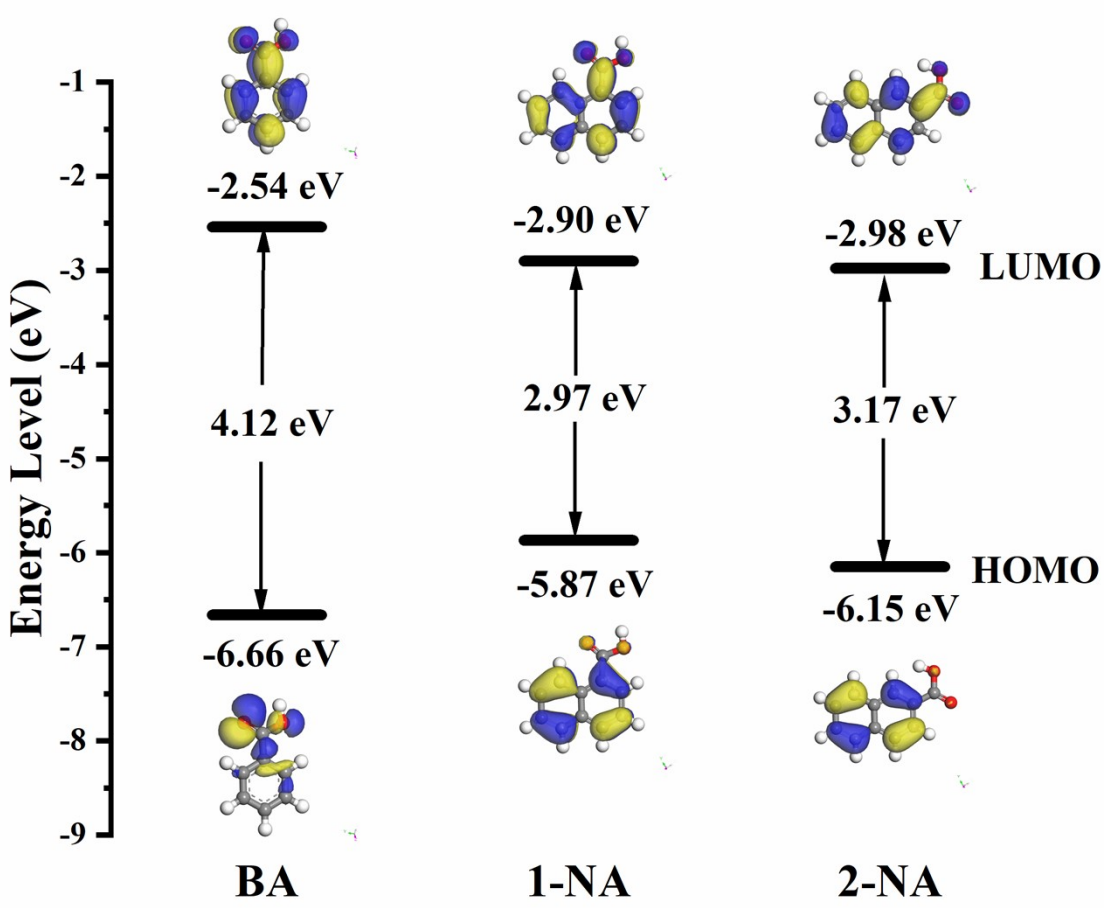

Fig. S2. DFT-calculated frontier molecular orbital energy level diagram.

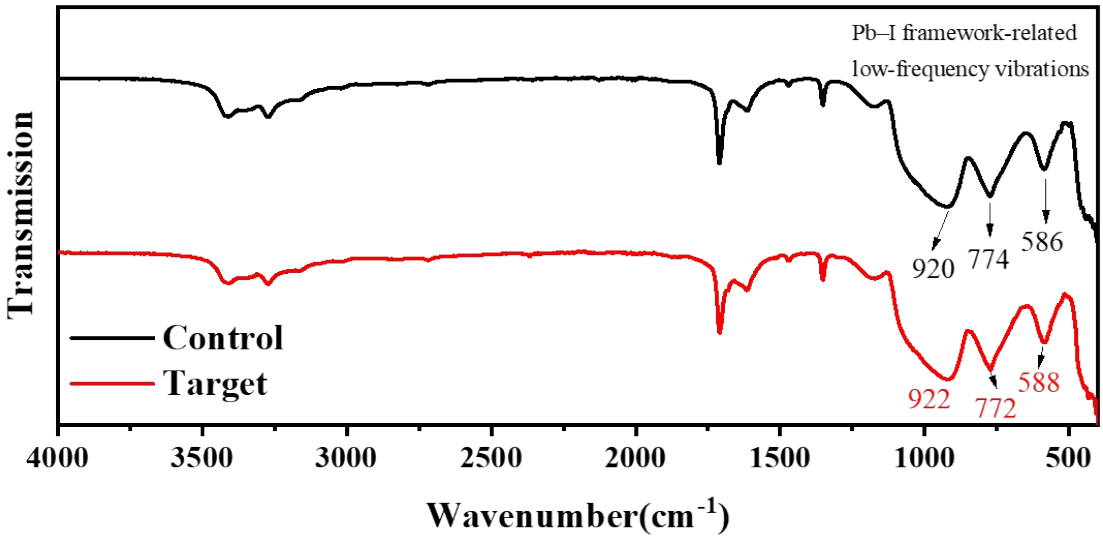

Fig. S3. FTIR spectra of the control and target perovskite films.

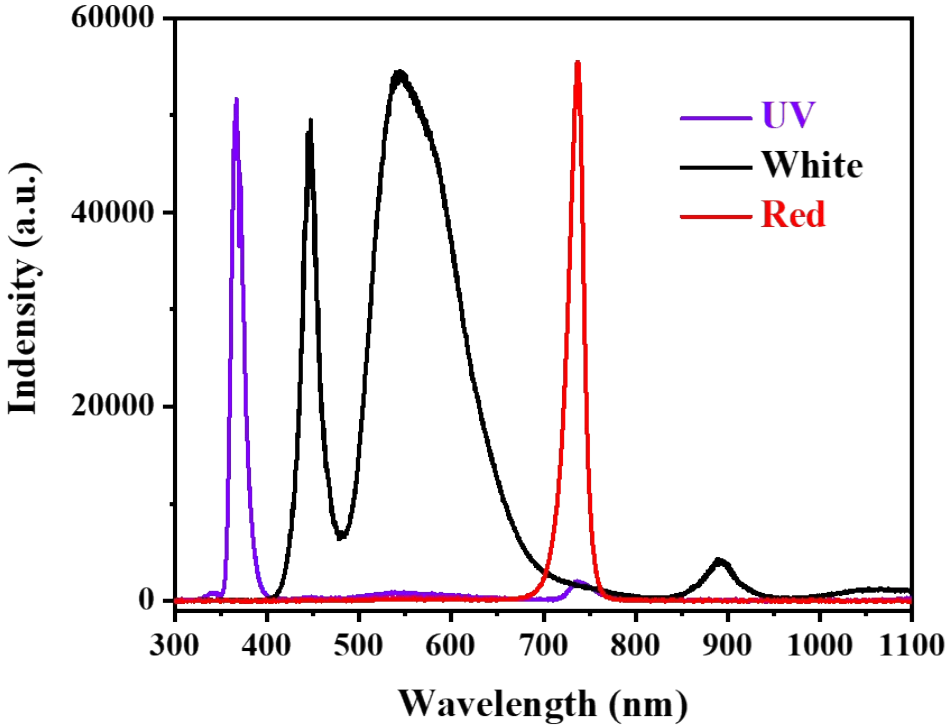

Fig. S4. The spectra of LED lamps for stability testing used in this study are: ultraviolet (UV) LED lamp (365 nm), white LED lamp (445 nm and 545 nm), and red LED lamp (730 nm).

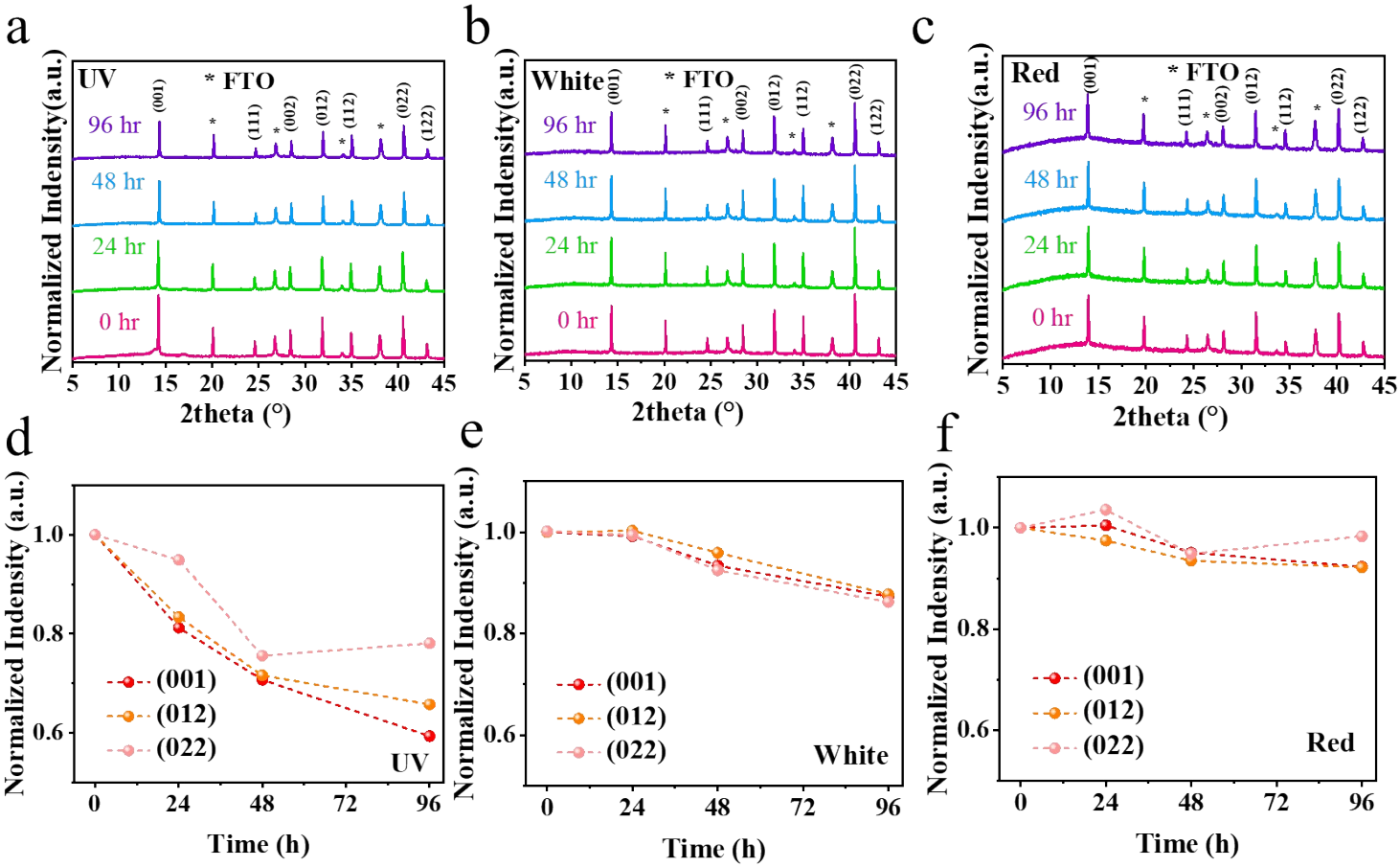

Fig. S5. XRD spectra of the perovskite films under 100 mW/cm² (a) UV, (b) white, and (c) red LED aging at different time intervals. (d-f) Attenuation of the XRD peak intensity for the (001), (012), and (022) planes of the perovskite film under aging with three different light sources.

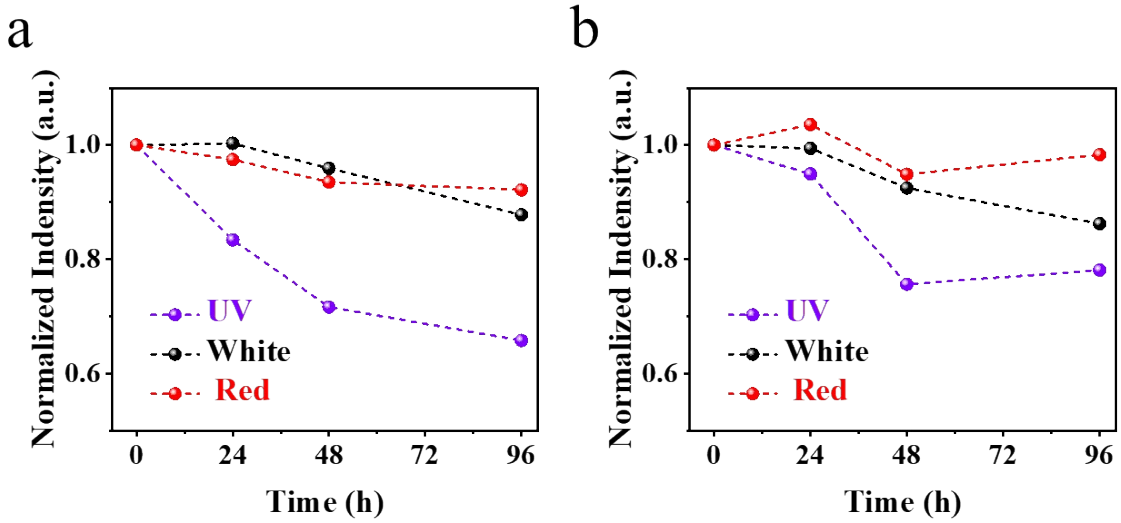

Fig. S6. Attenuating the XRD peak intensity for the (a) (012) and (b) (022) planes of perovskite films under 100 mW/cm² UV, white, and red LED aging (~30 ℃), respectively.

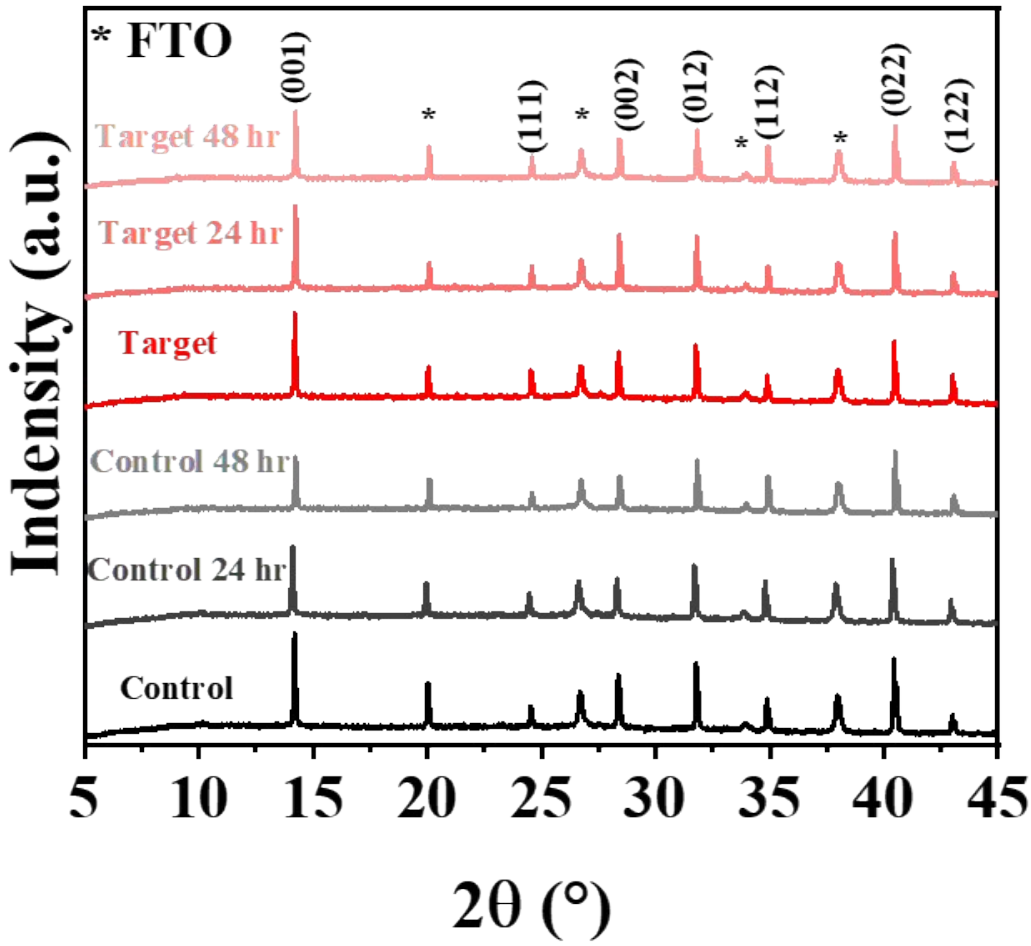

Fig. S7. XRD spectra of the control and target (with 1-NA) perovskite films under 150 mW/cm² UV aging (~30 ℃).

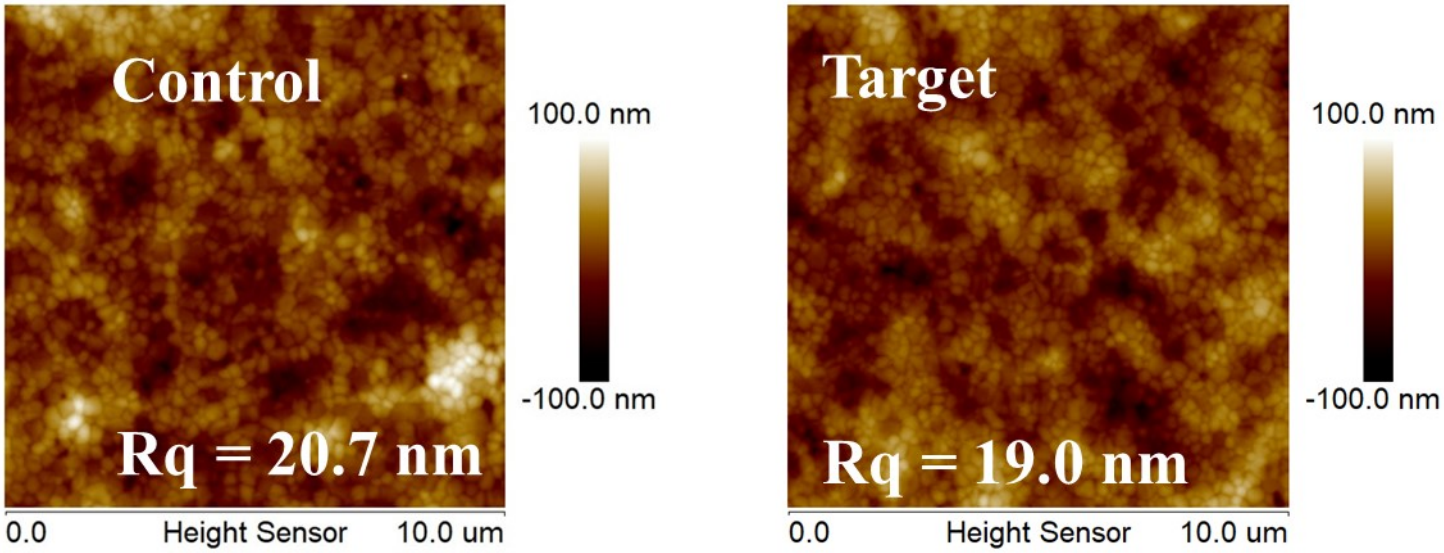

Fig. S8. Atomic force microscope (AFM) images of the control and target perovskite films.

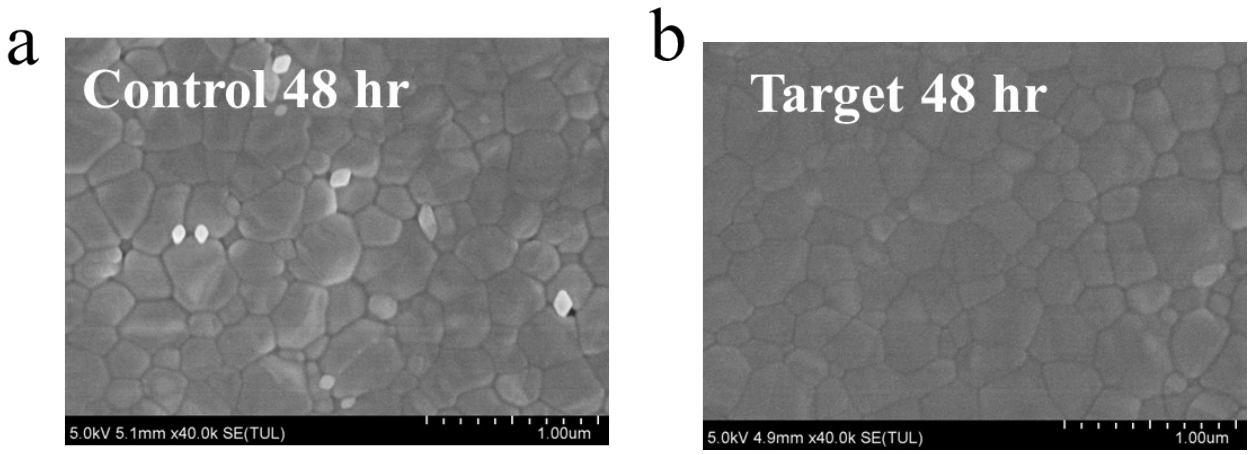

Fig. S9. Top-view SEM images of perovskite films: (a) control after 48 hours, (b) target after 48 hours of 50 mW/cm² UV aging.

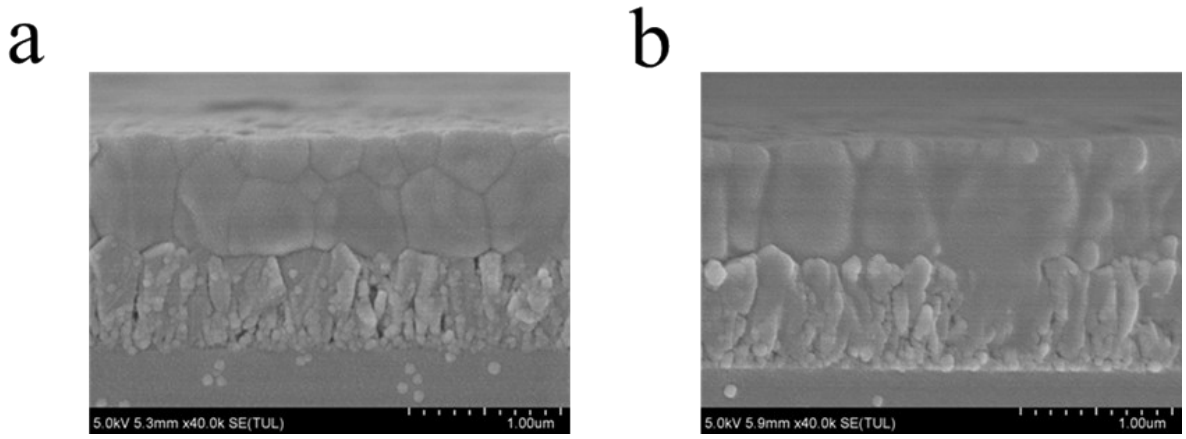

Fig. S10. Cross-sectional SEM images of the (a) control (774 nm) and (b) target (784 nm) perovskite films.

a

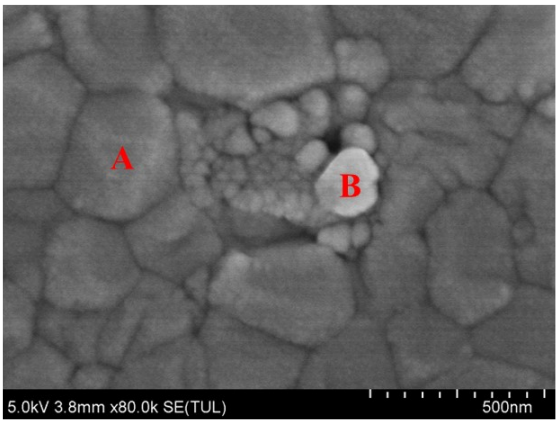

b

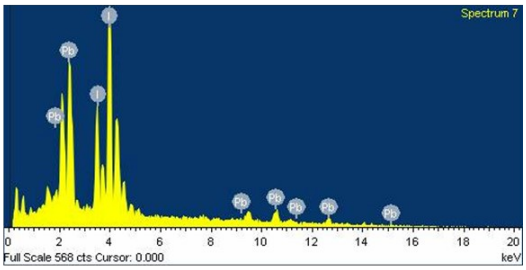

c

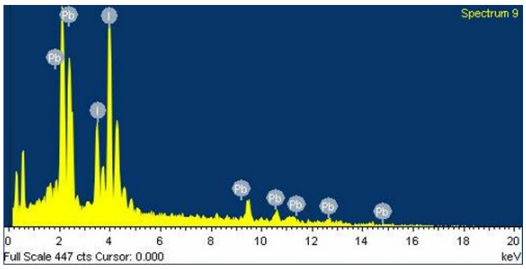

d

Element(Atomic%)	Pb	I	I/Pb
Point A	25.13	74.87	2.98
Point B	27.96	72.04	2.58

Fig. S11. (a)Top-view SEM images of perovskite films: control after 96 hours of 50 mW/cm² UV aging. (b-d) EDS spectrum results of the Point A and B.

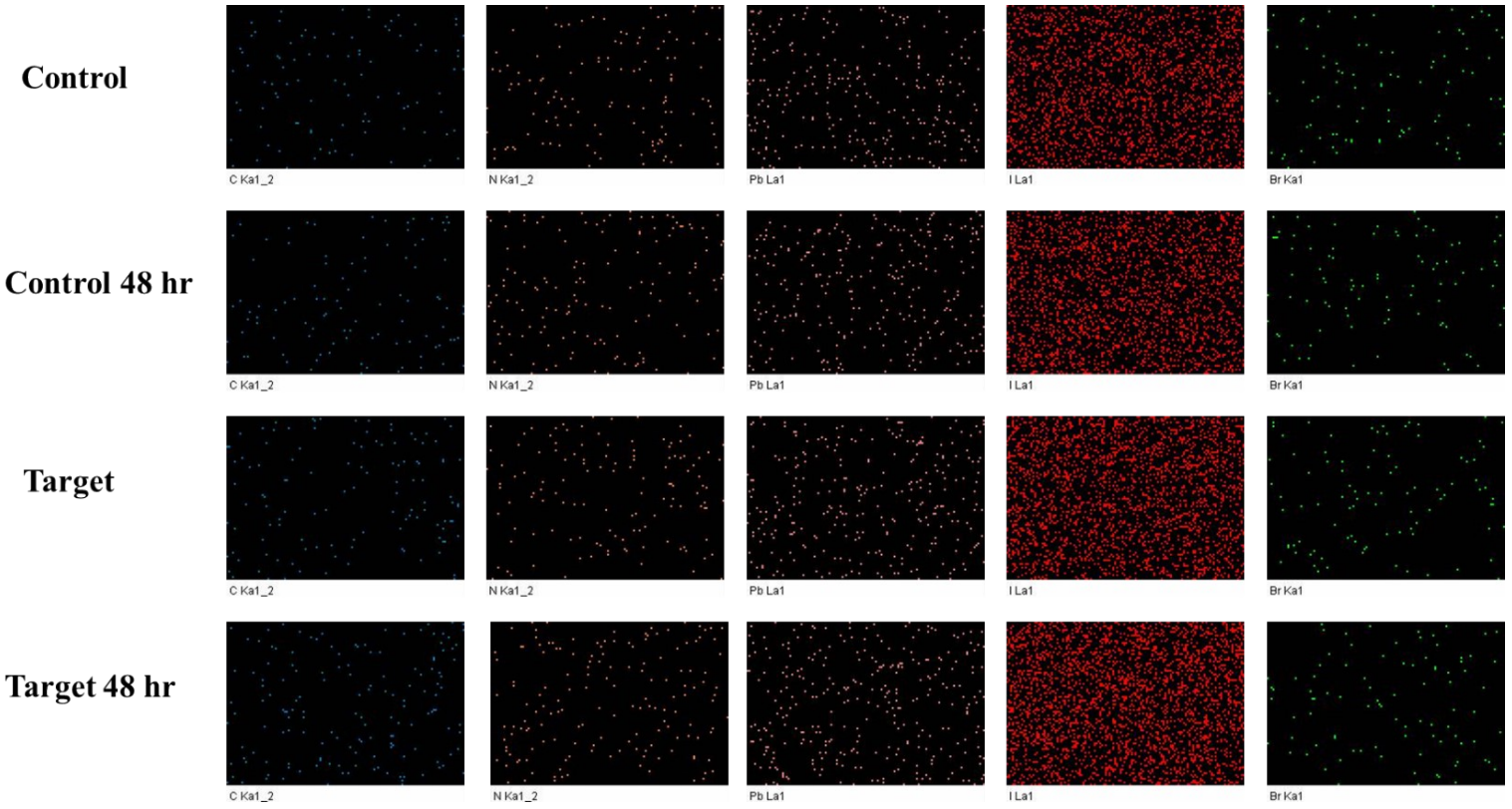

Fig. S12. EDS spectrum of the surface of perovskite films (20,000x scale): before and after 48 hours of 50 mW/cm² UV aging.

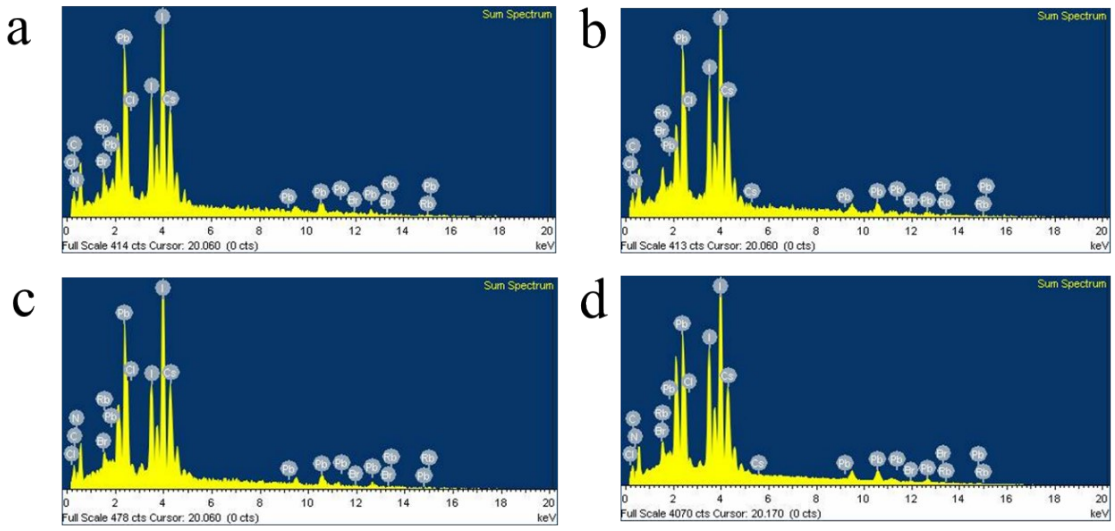

e

Element(Atomic%)	C	N	Pb	I	Br	N/C	I/Pb
Control	31.43	31.06	9.11	26.24	2.15	0.99	2.88
Control aging	31.17	21.47	9.97	28.06	3.33	0.69	2.81
Target	28.48	30.44	10.15	29.13	1.80	1.06	2.87
Target aging	27.88	26.74	10.7	31.92	2.76	0.96	2.98

Fig. S13. EDS spectrum results: (a) control, (b) control after 48 hours of 50 mW/cm² UV aging, (c) target, and (d) target after 48 hours of 50 mW/cm² UV aging. (e) EDS results of the surface of perovskite films.

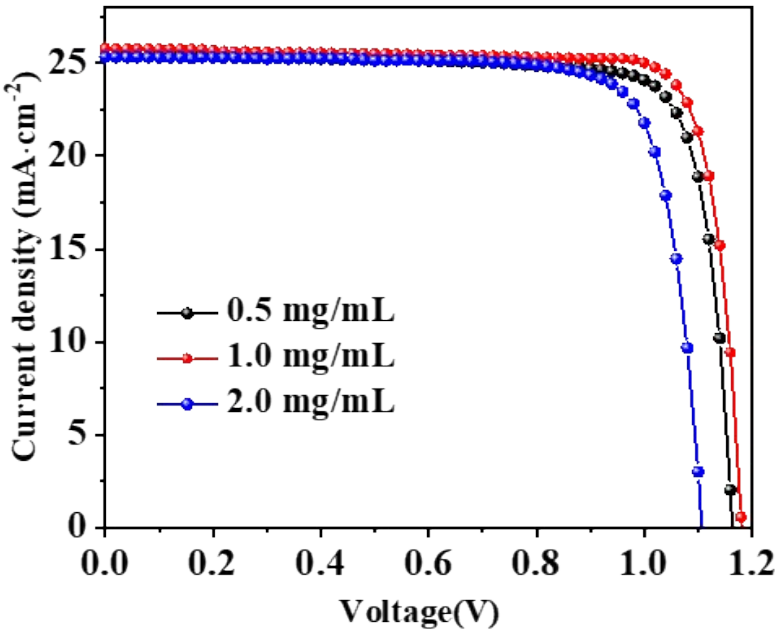

Fig. S14 *J-V* curves of the PSCs treated with gradient 1-NA concentrations.

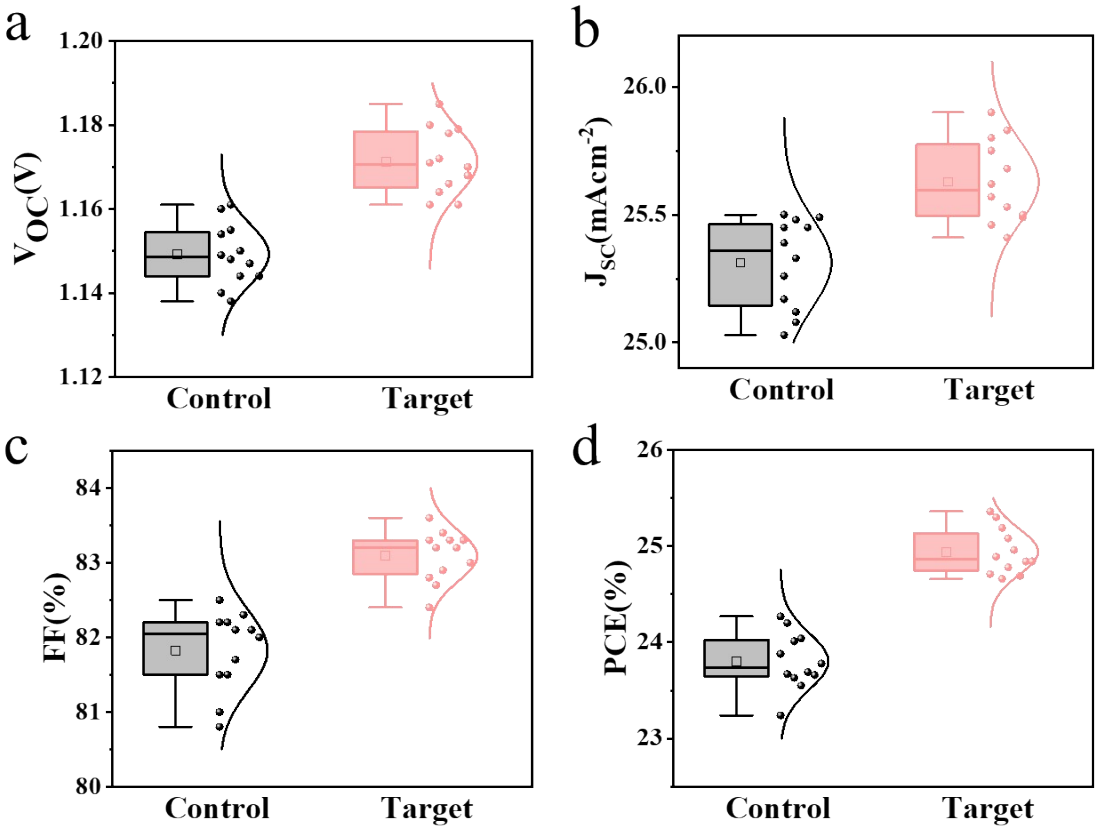

Fig. S15. Statistical photovoltaic parameters of control and target devices. The box plots display the mean, median line, 25~75% box limits with 1.5× interquartile range whiskers. a) V_{OC}. b) J_{SC}. c) FF. d) PCE.

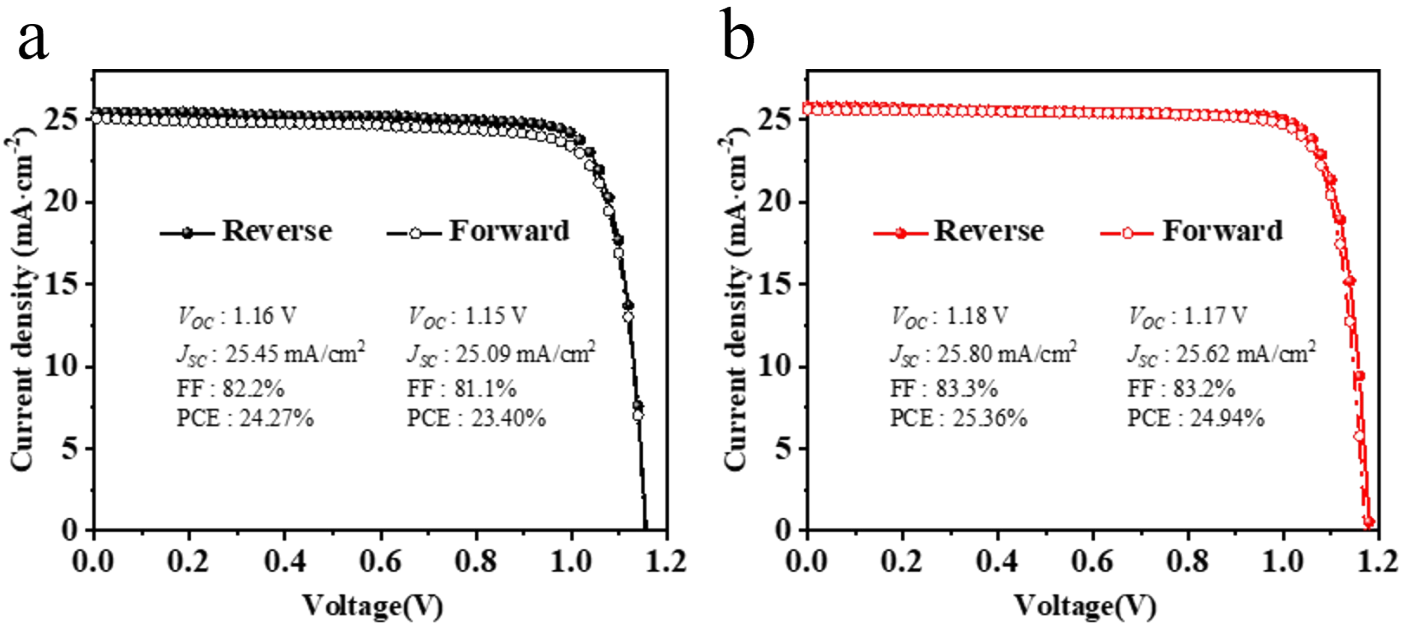

Fig. S16. *J-V* curves of the PSCs treated without (a) and with (b) 1-NA under reverse and forward scanning directions.

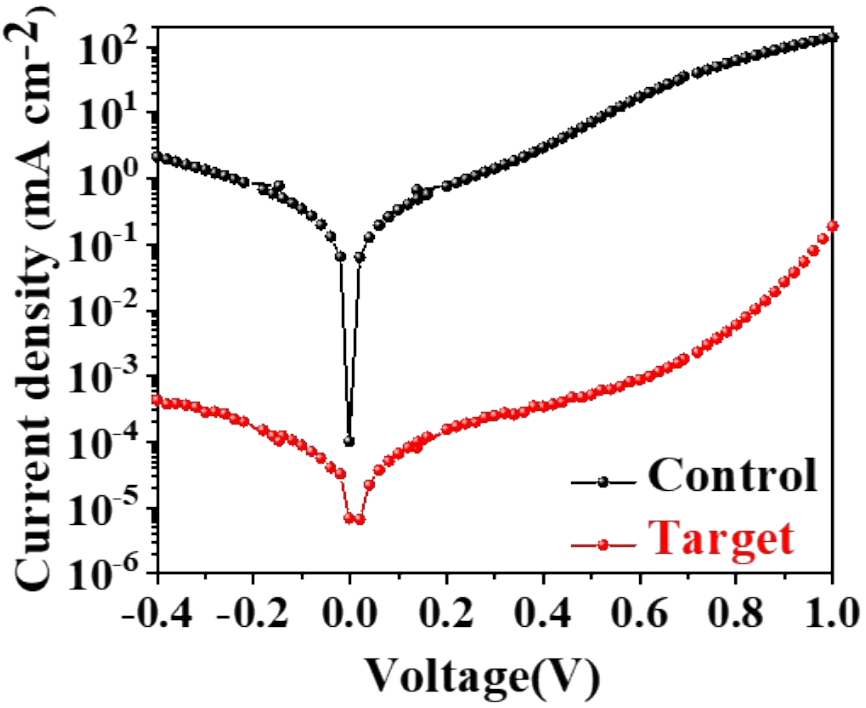

Fig. S17. Dark *J-V* curves of the control and target perovskite films.

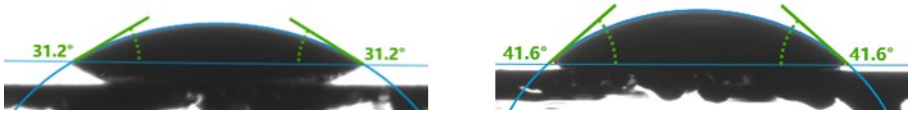

Fig. S18. Water contact angle of perovskite films: control (left) and target (right).

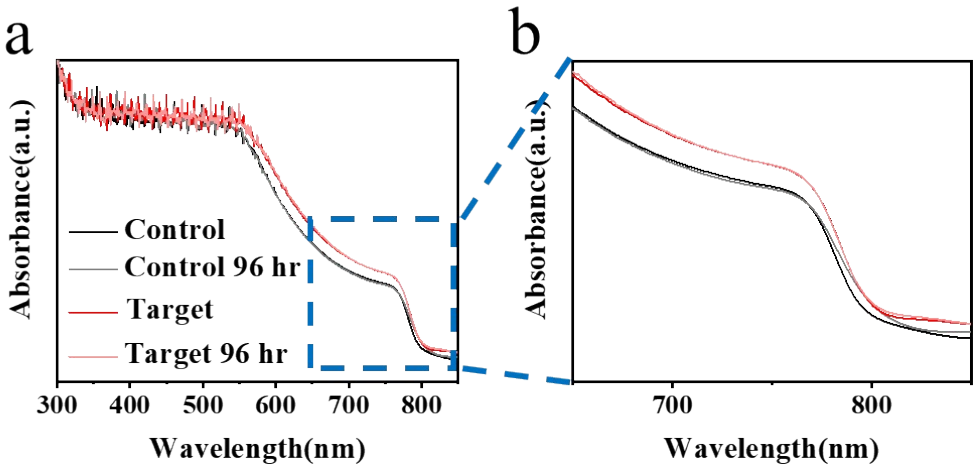

Fig. S19. UV-Vis absorption spectrum of the control and target perovskite films before and after 96 hours of UV aging (50 mW/cm^2, ~30 °C).

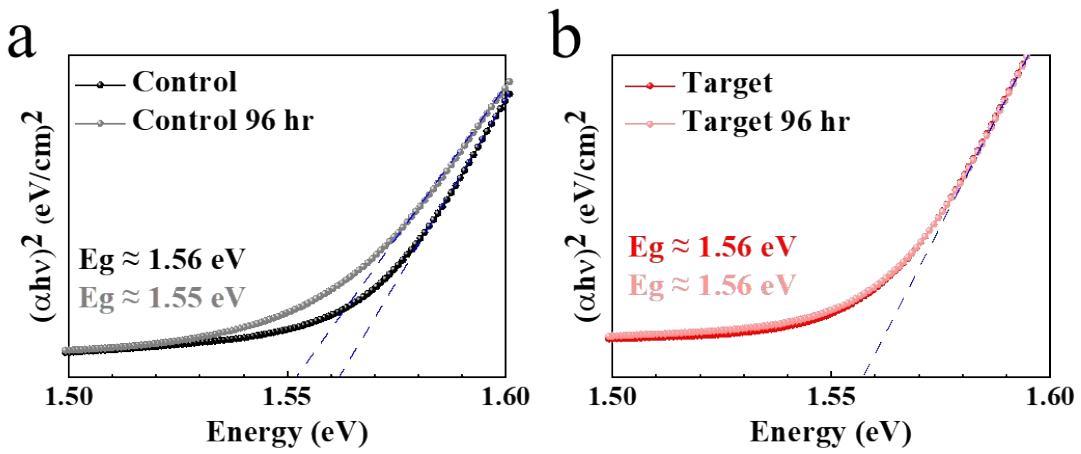

Fig. S20. Tauc plot of the control and target perovskite films before and after 96 hours of UV aging.

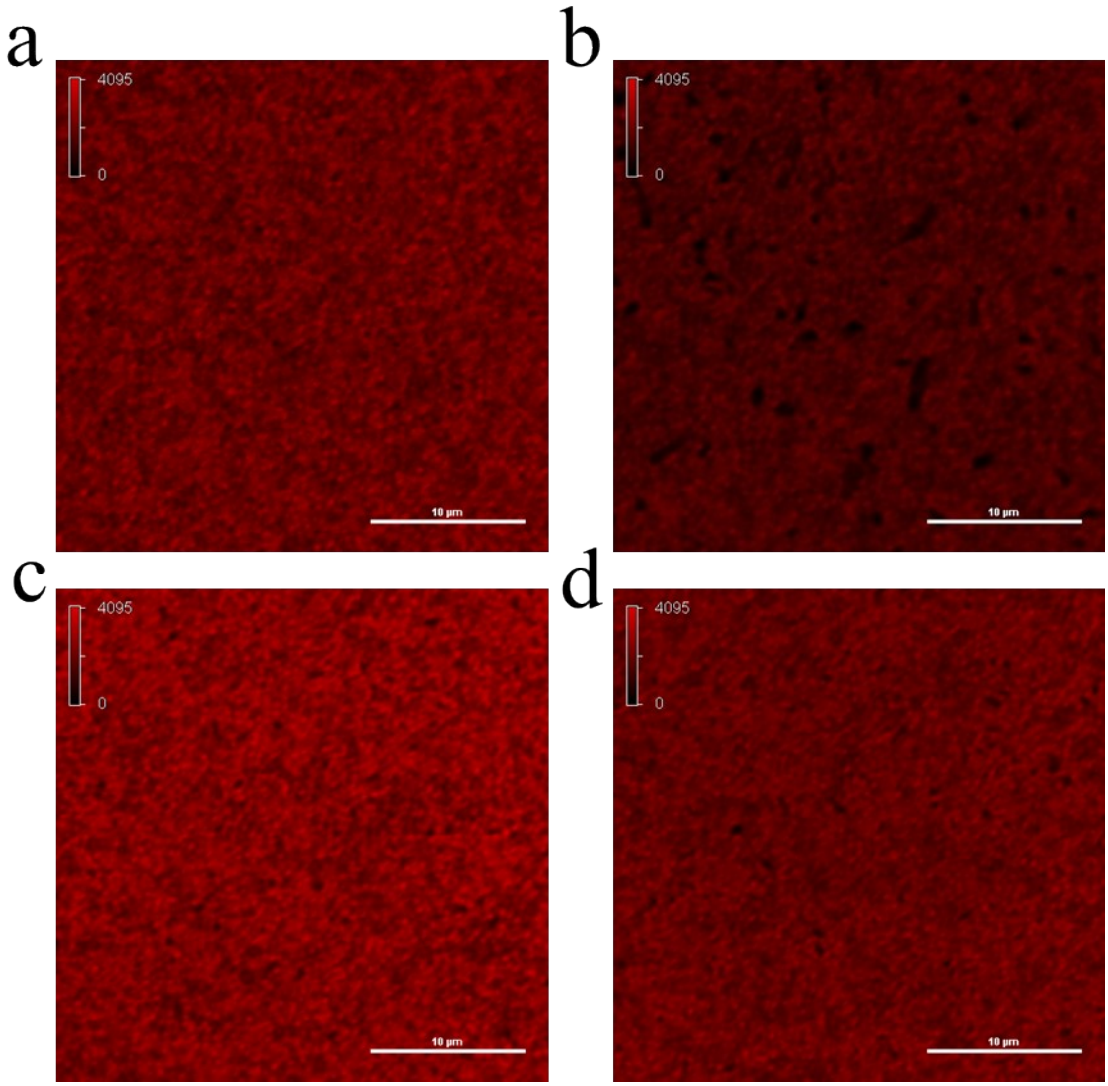

Fig. S21. PL mapping results of the control (a,b) and target (c,d) perovskite films before and after 96 hours of UV aging (50 mW/cm^2, ~30 °C).

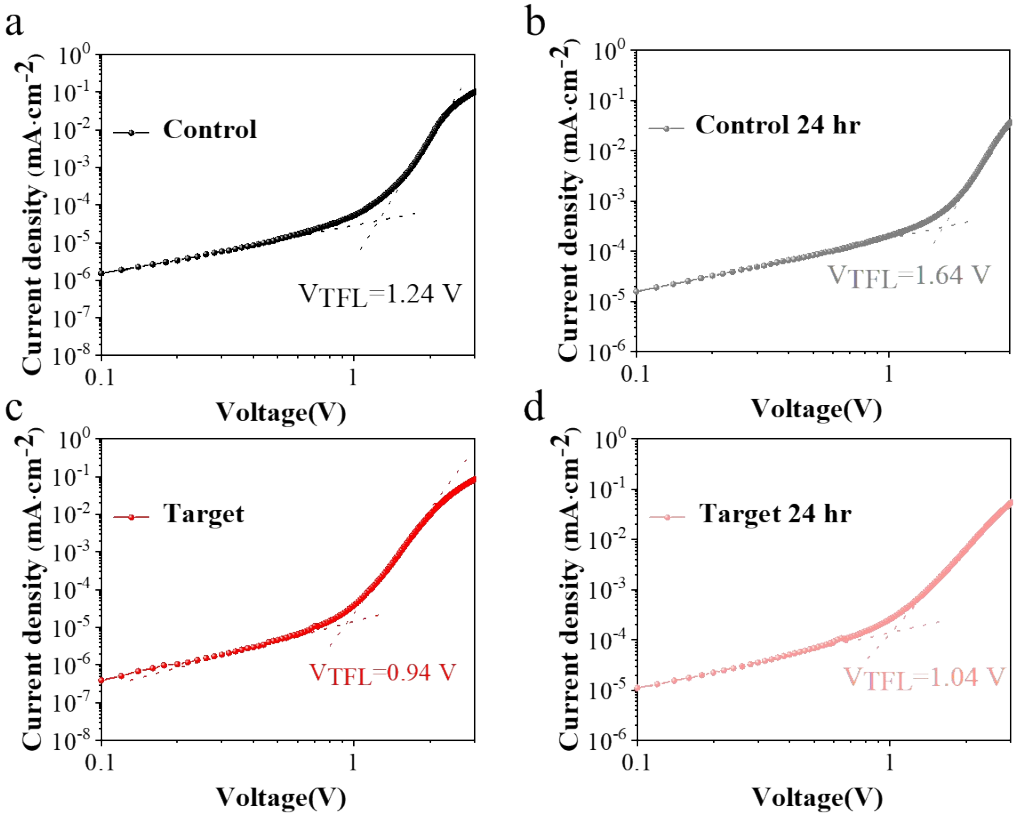

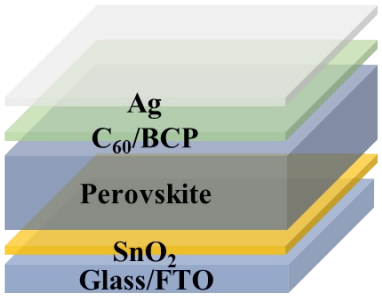

f

Device	N_t [cm^{-3}]
Control	1.01×10^{16}
Control 24 hr	1.38×10^{16}
Target	7.64×10^{15}
Target 24 hr	8.47×10^{15}

Fig. S22. (a-d) SCLC curves of the control and target perovskite films before and after 24 hours of UV aging (100 mW/cm^2, ~30 ℃). (e) The schematic structure of electron-only devices for SCLC. (f) The calculated trap density (N_t) from SCLC curves for the electron-only devices.

Supplementary Tables

Table S1. Transient resolved carrier lifetime fitting for Fig. 5b.

Sample	A_1	τ_1(ns)	A_2	τ_2(ns)	τ_{avg}(μs)
Control	147.697	4.027	823.948	2178.742	1.85
Control 96 hr	481.569	59.159	463.43	599.588	0.32
Target	200.024	37.167	656.293	3803.768	2.92
Target 96 hr	385.936	77.968	546.45	1304.968	0.80